Chemosphere 291 (2022) 133001

Contents lists available at ScienceDirect

Chemosphere

journal homepage: www.elsevier.com/locate/chemosphere

Construction of Bi_2WO_6/CoAl-LDHs S-scheme heterojunction with efficient photo-Fenton-like catalytic performance: Experimental and theoretical studies

Binbin Shao, Zhifeng Liu [*], Lin Tang [**], Qinghua Liang, Qingyun He, Ting Wu, Yuan Pan, Min Cheng, Yang Liu, Xiaofei Tan, Jing Tang, Hou Wang, Haopeng Feng, Shehua Tong

College of Environmental Science and Engineering, Hunan University and Key Laboratory of Environmental Biology and Pollution Control (Hunan University), Ministry of Education, Changsha, 410082, PR China

HIGHLIGHTS

- Hortensia-like Bi_2WO_6/CoAl-LDHs composite was synthesized via hydrothermal process.
- Optical-electrical properties and H_2O_2 adsorption behavior of samples were calculated by DFT.
- Bi_2WO_6/CoAl-LDHs composite exhibited high photo-Fenton-like catalytic activity of antibiotic.
- An internal electric field and S-scheme heterojunction form between Bi_2WO_6 and CoAl-LDHs.

GRAPHICAL ABSTRACT

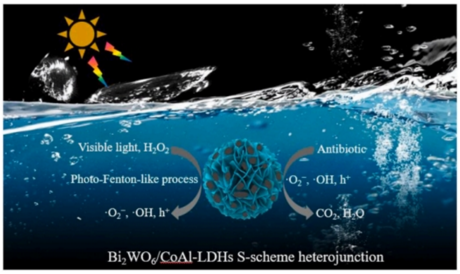

ARTICLE INFO

Handling Editor: Chang Min Park

Keywords:
Photo-fenton-like catalytic
Antibiotic contamination
Layered double hydroxides
Internal electric field
S-scheme heterojunction

ABSTRACT

The photo-Fenton-like catalytic process has shown great application potential in environmental remediation. Herein, a novel photo-Fenton-like catalyst of Bi_2WO_6 nanosheets decorated hortensia-like CoAl-layered double hydroxides (Bi_2WO_6/CoAl-LDHs) was synthesized via hydrothermal process. The optimized Bi_2WO_6/CoAl-LDHs composite performed the high-efficiency photo-Fenton-like catalytic performance for oxytetracycline (OTC) removal (98.47%) in the mediation of visible-light and H_2O_2. The comparative experiment, technical characterization and density functional theory calculation results indicated that the efficient photo-Fenton-like catalytic performance of Bi_2WO_6/CoAl-LDHs was attributed to the synergistic action of the Fenton-like process of cobalt ions in CoAl-LDHs, an internal electric field and the S-scheme heterojunction form between Bi_2WO_6 and CoAl-LDHs, which could significantly promote the active substance formation and the photocatalytic process in the catalytic system. This study will stimulate the new inspiration of designing the efficient catalytic system for environmental remediation and other fields.

---

[*] Corresponding author. College of Environmental Science and Engineering, Hunan University and Key Laboratory of Environmental Biology and Pollution Control (Hunan University), Ministry of Education, Changsha, 410082, PR China.

[**] Corresponding author. College of Environmental Science and Engineering, Hunan University and Key Laboratory of Environmental Biology and Pollution Control (Hunan University), Ministry of Education, Changsha, 410082, PR China.

E-mail addresses: zhifengliu@hnu.edu.cn (Z. Liu), tanglin@hnu.edu.cn (L. Tang).

https://doi.org/10.1016/j.chemosphere.2021.133001
Received 8 October 2021; Received in revised form 17 November 2021; Accepted 18 November 2021

1. Introduction

Over the past decades, the development of advanced oxidation processes (AOPs) for environmental remediation has obtained great attention, which includes ozonation, electrocatalysis, photocatalysis, Fenton catalytic and so on (Shao et al., 2020a; Zhou et al., 2020; Lu et al., 2020; Wu et al., 2020a). Many studies have indicated that the AOPs can effectively deal with environmental pollutants, includes organic pollution (eg. phenols, dyes, antibiotics), inorganic pollution (eg. heavy metals), pathogenic bacteria (eg. *Escherichia coli*, *Staphylococcus aureus*) (Zhou et al., 2020; Chen et al., 2017; Shao et al., 2017, 2019a). Among these methods, the photocatalysis techniques should be a promising remediation technology due to their environment-friendly and high-efficiency nature (Liu et al., 2019; Shao et al., 2018, 2019b). Up to now, a variety of photocatalytic materials have been researched, including metal oxide, metallic sulfide, oxyhalogenide and metal-free materials (Shao et al., 2020b; Wu et al., 2020b; Huang et al., 2020; Zhang et al., 2020a). Although such photocatalysts exhibited a considerable photocatalytic performance for contaminants removal, they are still far from practical application because of their some pertinacious disadvantages, such as poor photostability, expensive, and the rapid recombination of photoinduced electron-hole pairs (e^--h^+) (Pan et al., 2020; Liu et al., 2020a; Liang et al., 2020; Duan et al., 2020). Therefore, continuous efforts have been employed to enhance the photocatalytic performance via element doping, morphological design, building heterojunction and loading co-catalysts (Shao et al., 2019b, 2019c, 2020a). These strategies can significantly enhance the photocatalytic performance of photocatalysts and improve their practical potential.

Recently, the classic 2D materials of layered double hydroxides (LDHs, $[M_{1-x}^{2+}M_x^{3+}(OH)_2](A^{n-})^{x/n}\cdot mH_2O]$, the M^{2+} and M^{3+} are divalent (Mg^{2+}, Co^{2+} etc.) and trivalent metals (Al^{3+}, Fe^{3+} etc.), respectively, A^{n-} is a charge-balancing anion (CO_3^{2-} etc.)), have attracted considerable attention because of their excellent physical-chemical properties and low-cost (Kumar et al., 2017; Wu et al., 2018; Xia et al., 2020a; Wang et al., 2018a). Typically, the LDHs comprise positively charged layers of edge-sharing MO_6 octahedra with charge compensating anions between the interlayers, and the CoAl-LDHs are common LDHs and widely studied in photocatalysis, electrocatalysis, adsorption, energy storage and other fields recently (Xia et al., 2020a; Wang et al., 2018a). Shao et al. (Xu et al., 2015; Shao et al., 2021a; Peng et al., 2020) reported that the band gap of CoAl-LDHs is about 2.4 eV, which indicates that the CoAl-LDHs are well responsive to visible light and should be a promising visible-light photocatalyst. However, Wu et al. (Kumar et al., 2017; Wu et al., 2018; Xia et al., 2020a; Shao et al., 2021a) found that the pristine CoAl-LDHs generally suffer slow charge carrier mobility and rapid e^--h^+ recombination, thus inhibiting its photocatalytic performance. For solving this problem, combining CoAl-LDHs with other semiconductor materials to construct a heterostructure composite should be an effective strategy. For instance, Xia et al. (2020a) prepared a core-shell morphologic Z-scheme heterojunction of CeO_2/CoAl-LDHs for visible-light photodegradation of gaseous formaldehyde. In comparison to the bare CoAl-LDHs, the composite performed the higher conversion efficiency of formaldehyde, and the maximum efficiency over 87% was achieved. Kumar et al. (2017) also reported that the p-n heterojunction of P25@CoAl-LDHs nanohybrids performed the better photoreduction activity and selectivity (>90%) for CO_2 than the CoAl-LDHs. It was certain that the construction of heterojunction material can significantly promote charge transfer, improve light utilization of CoAl-LDHs, thus improving they photocatalytic performance. Compared with the Z-scheme and p-n heterojunction, the newly proposed step-scheme (S-scheme) heterojunction exhibits more efficient photocatalytic performance, and has become the research hotspot recently (Xu et al., 2020; Tao et al., 2021; Xia et al., 2020b). For instance, Tao et al. (2021) had constructed a S-scheme heterojunction of MoS_2/CoAl-LDHs, and the photocatalytic hydrogen evolution performance of optimized MoS_2/CoAl-LDHs heterojunction was 7.4 times higher than that of pure CoAl-LDHs. Among the photocatalytic materials, the Bi_2WO_6 should be a promising photocatalyst due to their narrow band gap (about 2.7 eV), stable physical-chemical properties, low cost, and non-toxicity (Wang et al., 2017). To date, various Bi_2WO_6 based heterostructure photocatalysts have been constructed, such as $g\text{-}C_3N_4/Bi_2WO_6$ (Wang et al., 2017), Ti_3C_2/Bi_2WO_6 (Cao et al., 2018), black phosphorus/Bi_2WO_6 (Hu et al., 2019). However, there is still a lack of research on the S-scheme heterojunction of Bi_2WO_6/CoAl-LDHs in environmental remediation so far.

Furthermore, considering the high oxidizability of Fenton reaction and some commonalities between Fenton reaction and photocatalytic reaction (the produce of reactive oxygen species (ROS), usually hydroxyl radicals ($\cdot OH$)), recently, the synergetic photo-Fenton process have been well regarded as a more efficient catalytic process compared to the single photocatalytic process (Han et al., 2020). For instance, Zhou et al. (2020) constructed an efficient photo-Fenton system based on a Z-scheme composite ($TiO_2/Pt/MoS_2$), and this coupling catalytic system showed the excellent degradation for organic contaminants and reduction for metal ions. Generally, the traditional homogeneous Fenton reaction process was employed Fe^{2+} to activate H_2O_2 thus generating $\cdot OH$ (equations (1) and (2)). However, the strict pH range (2–4), high cost and large amounts of produced solid sludge limit the practical application of homogeneous Fenton reaction (Han et al., 2020; Zhu et al., 2019). Therefore, the heterogeneous Fenton-like reaction (other kinds of catalysts are used to replace Fe^{2+}), which possesses high oxidizability, a wide range of reaction pH and inexpensive, has received more interest. Various Fenton-like reaction have been studied till now, such as Fe^{3+}/H_2O_2, Co^{2+}/H_2O_2, Ni^{2+}/H_2O_2, and Cu^{2+}/H_2O_2 (Zhu et al., 2019; Ren et al., 2020; Cheng et al., 2018). In addition, the LDHs materials have been proved to be a good Fenton-like catalyst due to the presence of abundant transition metal ions (eg. Fe^{2+}, Fe^{3+}, Cu^{2+}, Co^{2+}) (Yang et al., 2020; Guo et al., 2020; Wang et al., 2018b). Recently, Guo et al. (2020) reported that the CoCu-LDHs could be as a high-efficiency Fenton-like catalyst for anthraquinones-containing H_2O_2 production effluent (AHE) treatment, and the highest COD and TOC removal of AHE was up to 89.9% and 71.3%, respectively, under the pH of 6.8. Wang et al. (2018b) also reported that the phenol could be effectively mineralized in the Fenton-like catalytic system by using the CuNiFe-LDHs as the catalyst. To sum up, the major advantages by using LDHs as the heterogeneous Fenton-like catalysts are as follows: (1) the plentiful divalent and trivalent metal ions and the layered structure of LDHs endowed them the abundant catalytic sites; (2) the valence state change of metal ions in octahedra cage and the strong metal synergetic interaction of LDHs during the Fenton-like reaction could restrain the leaching of the metal ions; (3) the LDHs performed the Fenton-like catalytic activity over a wide pH (Yang et al., 2020; Guo et al., 2020; Wang et al., 2018b).

$$Fe^{2+} + H_2O_2 \rightarrow Fe^{3+} + \cdot OH + OH^- \tag{1}$$

$$Fe^{3+} + H_2O_2 \rightarrow Fe^{2+} + \cdot OOH + H^+ \tag{2}$$

Motivated by the above studies, herein, we fabricated the S-scheme heterojunction of Bi_2WO_6/CoAl-LDHs via the hydrothermal process, in which the CoAl-LDHs were used as both photocatalyst and Fenton-like catalyst. Their photo-Fenton-like catalytic performance were investigated toward antibiotic degradation under visible-light illumination and H_2O_2 mediation. The physical-chemical and optical-electrical properties of obtained catalysts were explored through multiple characterization techniques. Meanwhile, the photocatalytic and Fenton-like catalytic mechanism for this photo-Fenton-like catalytic system were further studied by theoretical calculation base on the density functional theory (DFT). This study could provide a new inspiration for designing an efficient catalytic system for environmental remediation and other fields.

2. Experimental

2.1. Preparation of catalysts

The hortensia-like CoAl-LDHs (CA) were prepared by hydrothermal process (Jo and Tonda, 2019), in details, 0.873 g of $Co(NO_3)_2·6H_2O$ and 0.375 g of $Al(NO_3)_3·9H_2O$ were added into 70 mL of ultrapure water and stirred for 30 min to obtain a mixture. Then, 1.5 g of urea and 0.296 g of NH_4F were mixed with the above mixture, and continuous stirring for 60 min at room temperature to get a suspension. Subsequently, the suspension was transferred into a 100 mL Teflon-lined stainless-steel autoclave and heated at 120 °C for 24 h. Finally, the hortensia-like CoAl-LDHs were obtained.

The Bi_2WO_6/CoAl-LDHs composites were prepared as follows (Fig. 1): 0.97 g of $Bi(NO_3)_3·5H_2O$ and a certain amount of CoAl-LDHs were dispersed in 40 mL ultrapure water (Solution A). Meanwhile, 0.330 g of $Na_2WO_4·2H_2O$ and 0.055 g of CTAB were dissolved in 40 mL ultrapure water and stirred for 60 min (Solution B). Then solution A was slowly added into solution B and stirring for 60 min, after that, the mixed solution was transferred into a 100 mL Teflon-lined autoclave and kept at 120 °C for 24 h. The obtained residues were thoroughly washed and dried, the mass ratios of Bi_2WO_6 to CoAl-LDHs were set as 5%, 10%, 20% and 30%, and they were labeled as BWCA-5, BWCA-10, BWCA-20, BWCA-30, respectively. For comparison, the Bi_2WO_6 nanosheets were also prepared under the same procedure without the addition of CoAl-LDHs (Cao et al., 2018). Various characterization techniques had been employed for investigating the physical-chemical and optical-electrical properties of obtained catalysts, and the related information were showed in supplementary information (SI).

2.2. Photo-fenton-like catalytic test

The photo-Fenton-like catalytic performance of the obtained samples was studied toward the degradation of oxytetracycline hydrochloride (OTC) (10 mg/L). In details, 100 mg of catalyst was dispersed into 100 mL of OTC aqueous solution. Before catalytic tests, a 60 min dark adsorption test was carried out to reach adsorption-desorption equilibrium. After that, photo-Fenton-like catalytic tests were performed under visible-light irradiation (a 300 W Xenon lamp, $\lambda > 420$ nm) and the mediation of H_2O_2 (0 mM, 5 mM, 10 mM, 20 mM, 50 mM, 100 mM). The cycle experiments were carried out as follows: the reaction solution in the catalytic system was removed by centrifugation (8000 rpm, 5 min) after the completion of one-stage experiment, and then the residual catalyst was re-dispersed in 100 mL of OTC for the next catalytic experiment. In each catalytic process, 1 mL of sample was sucked out at regular intervals and then filtrated for concentration analysis. The concentration of OTC was analyzed by a Shimadzu UV–vis spectrophotometer (UV-2700) with absorbance at the characteristic peak of 353

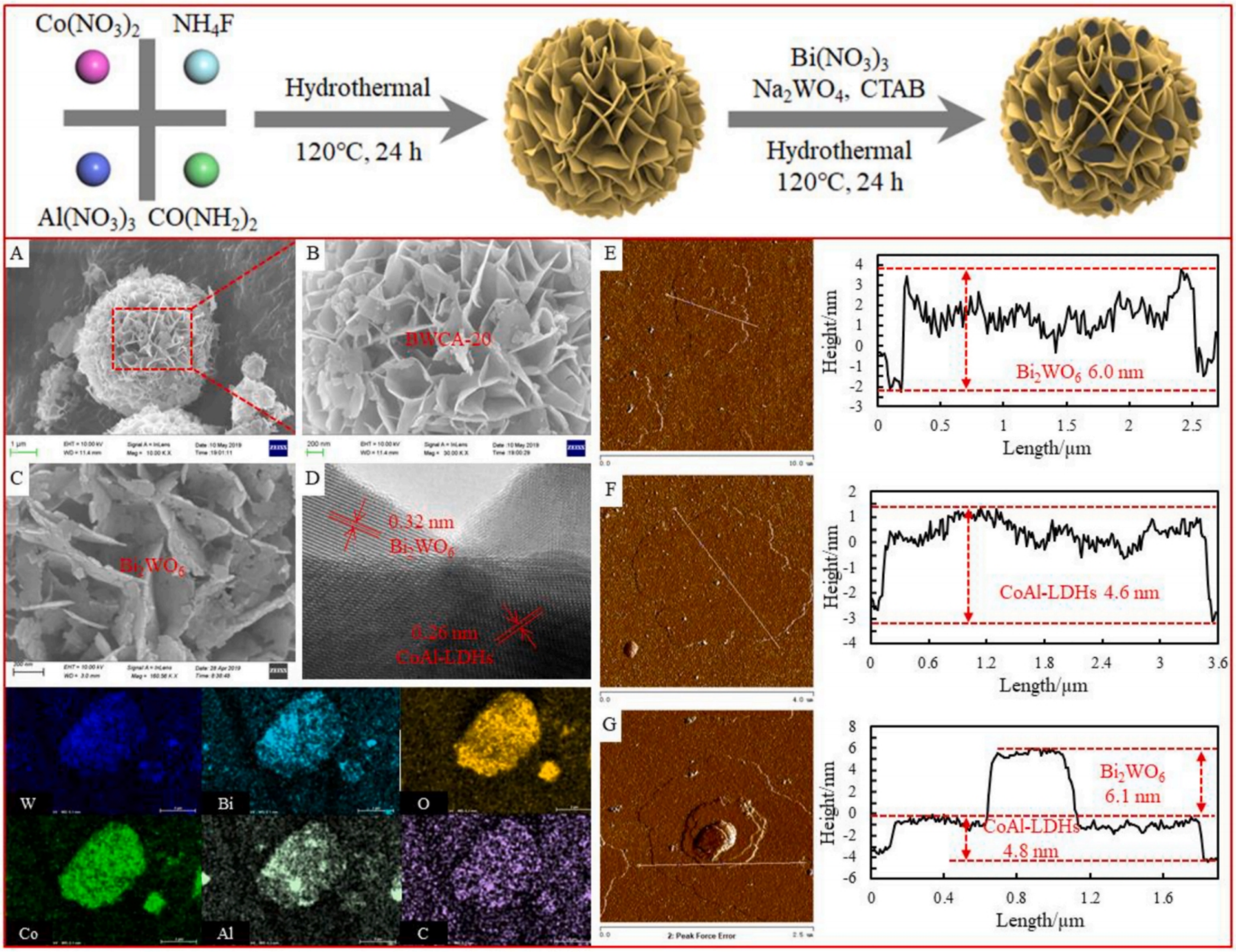

Fig. 1. Schematic illustration of the preparation process of the Bi_2WO_6/CoAl-LDHs composite; SEM, TEM and HRTEM images of as-prepared samples (A–D); AFM images and height profiles of the as-prepared samples (E–G); Corresponding elemental mapping images of BWCA-20 sample.

nm.

3. Results and discussion

3.1. Morphology, crystal, and chemical states

The morphology of obtained catalysts was analyzed by SEM, TEM and AFM measures. As shown in FESEM images (Fig. 1A–C), obviously, both Bi_2WO_6 and CoAl-LDHs were nanosheets structure, and the CoAl-LDHs showed the smoother surface than Bi_2WO_6. Besides, the CoAl-LDHs formed a hortensia-like morphology. As for the BWCA-20 nanohybrids (Fig. 1A–B), clearly, many irregular flakes were anchored on the surface of CoAl-LDHs, and they could be the Bi_2WO_6. The HRTEM image (Fig. 1D) further displayed that two kinds of lattice fringe were existed in the Bi_2WO_6/CoAl-LDHs nanohybrids, the lattice spacing of 0.26 nm and 0.32 nm correspond to the (012) plane of CoAl-LDHs and the (131) plane of Bi_2WO_6, respectively (Jo and Tonda, 2019; Wang et al., 2019). Additionally, the element distribution of BWCA-20 nanohybrids was further studied by elemental mapping, it was obvious that the Co, Al, Bi, W, C and O elements distributed evenly in the nanohybrids composite. Furthermore, the AFM results further exhibited the thickness of samples. As presented in Fig. 1E, the thickness of Bi_2WO_6 was about 6.0 nm, which is approximately 7–8 layers of Bi_2WO_6 nanosheets (Wang et al., 2017). For CoAl-LDHs sheets (Fig. 1F), their thickness was ~4.6 nm, indicating that the CoAl-LDHs sheets were about 5–6 layers (Wang et al., 2018a). As for the BWCA-20 (Fig. 1G), the lower height of 4.8 nm should be assigned to the CoAl-LDHs nanosheets, while the higher height of 6.1 nm could be ascribed to Bi_2WO_6 nanosheets. These AFM results confirmed that the obtained samples were few-layered nanosheets, and the Bi_2WO_6 nanosheets were randomly decorated on the surface of CoAl-LDHs.

The crystal phase of Bi_2WO_6, CoAl-LDHs and BWCA hybrids were analyzed via XRD, as presented in Fig. 2A. Obviously, the diffraction peaks of samples located at 28.3°, 32.8°, 47.3°, 56.1°, and 58.4° were corresponded to the (131), (200), (202), (133), and (262) crystal planes of orthorhombic Bi_2WO_6 (No. 39–0256), respectively (Wang et al., 2017). For the CoAl-LDHs, the diffraction peaks appeared at $2\theta = 11.7°$, 24.1°, 34.8°, 39.3°, and 46.9° were agreed with the (003), (006), (009), (012), and (018) lattice planes of the pure CoAl-LDHs reference (No. 38–0487) with CO_3^{2-} in the interlayer region (Kumar et al., 2017; Wu et al., 2018). In the XRD patterns of five nanohybrids, both of Bi_2WO_6 and CoAl-LDHs dominating phases were presented, and the peak intensity varies with the content. The above results manifested the combination of Bi_2WO_6 and CoAl-LDHs in a high purity and crystallinity status.

The typical functional groups of obtained samples were investigated via FTIR spectra. As shown in Fig. 2B, the absorption at 2366 cm^{-1} for all samples ascribed to the antisymmetric C=O stretching due to the atmospheric CO_2 (Ahmad and Kumar, 2010). In the spectrum of Bi_2WO_6, the peaks at 3400 and 1623 cm^{-1} are attributed to O–H vibrations. In addition, the peaks at 849, 730 and 580 cm^{-1} should be corresponded to the Bi–O, W–O stretching and Bi–O–Bi asymmetric stretch, respectively (Jo et al., 2018). For the CoAl-LDHs, the broad peak centered at 3400 cm^{-1} corresponded to the O–H stretching vibration of interlayer water molecules and H-bonded OH group, companied with the bending mode at 1647 cm^{-1} (Zhang et al., 2012). The peak at 1548 cm^{-1} was indicative of the H–O–H (δ-H_2O) deformation vibration (Chen et al., 2019). The peak at 1062 cm^{-1} due to typical bending vibrations of M-O-C bond (M represents Co or Al) (Jo and Tonda, 2019; Zhang et al., 2017). The peaks at 1355 cm^{-1}, 840 cm^{-1} and 964 cm^{-1} were due to the ν_3 stretching vibration and the bending modes of CO_3^{2-} (Chen et al., 2019). The troughs located in the low-frequency region (550-810 cm^{-1}) were generally corresponding to the stretching and bending vibration of M – O, O-M-O and M-O-M the crystals (Chen et al., 2019; Peng et al., 2017). As for the Bi_2WO_6/CoAl-LDHs nanohybrids, they showed both the characteristic absorption peaks of Bi_2WO_6 and CoAl-LDHs. Meanwhile, their FTIR spectrums were more close to that of CoAl-LDHs, which could attribute to the truth that the CoAl-LDHs were the main components in the nanohybrids.

The composition and chemical bonds of as-prepared samples were further determined via XPS analysis. According to the XPS survey spectra (Fig. S1), the BWCA-20 nanohybrid mainly contained Co, Al, Bi, W, C, F, N and O elements. Furthermore, the high-resolution XPS spectra of Bi 4f, W 4f, Al 2p, Co 2p, O 1s and C 1s were revealed. As displayed in Fig. 3A, clearly, the peaks at 165.11 eV and 159.75 eV of Bi 4f spectra corresponded to Bi $4f_{5/2}$ and Bi $4f_{7/2}$ of the Bi^{3+} ions in Bi_2WO_6, respectively (Wang et al., 2018c; Liang et al., 2021a). The W 4f spectrum (Fig. 3B) comprises of two peaks (37.39 eV and 34.45 eV) belonging to W $4f_{5/2}$ and W $4f_{7/2}$ of W^{6+}, respectively (Jo et al., 2018). Fig. 3C revealed the characteristic binding energy peak of Al 2p at 74.56 eV, suggesting that Al was in the +3 oxidation state in the samples (Islam et al., 2019). The Co 2p spectra (Fig. 3D) included four characteristic peaks, the binding energy at 781.99 eV, 798.09 eV corresponded to Co $2p_{3/2}$ and Co $2p_{1/2}$, respectively. Meanwhile, the shake-up satellites appeared at 786.52 eV and 803.79 eV, respectively (Jo and Tonda, 2019). The O 1s spectra was shown in Fig. 3E, it was observed that the O 1s for Bi_2WO_6/CoAl-LDHs could be fitted to four characteristic peaks at 529.31 eV, 530.85 eV, 532.25 eV and 534.88 eV. The peaks at 529.31 eV

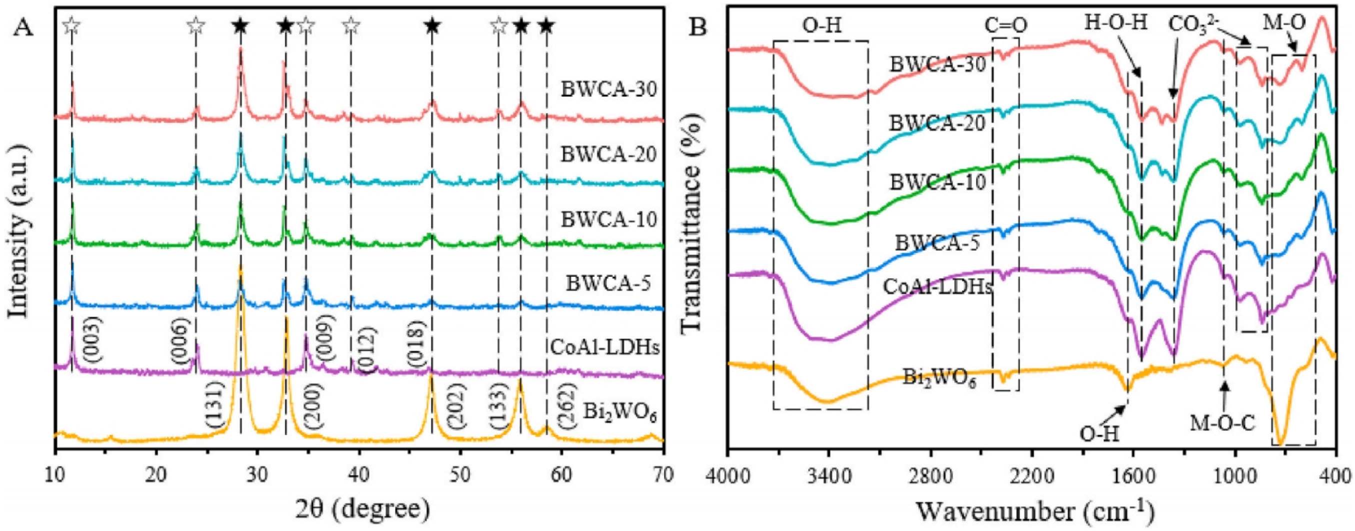

Fig. 2. XRD patterns (A) and FTIR spectra (B) of the as-prepared samples.

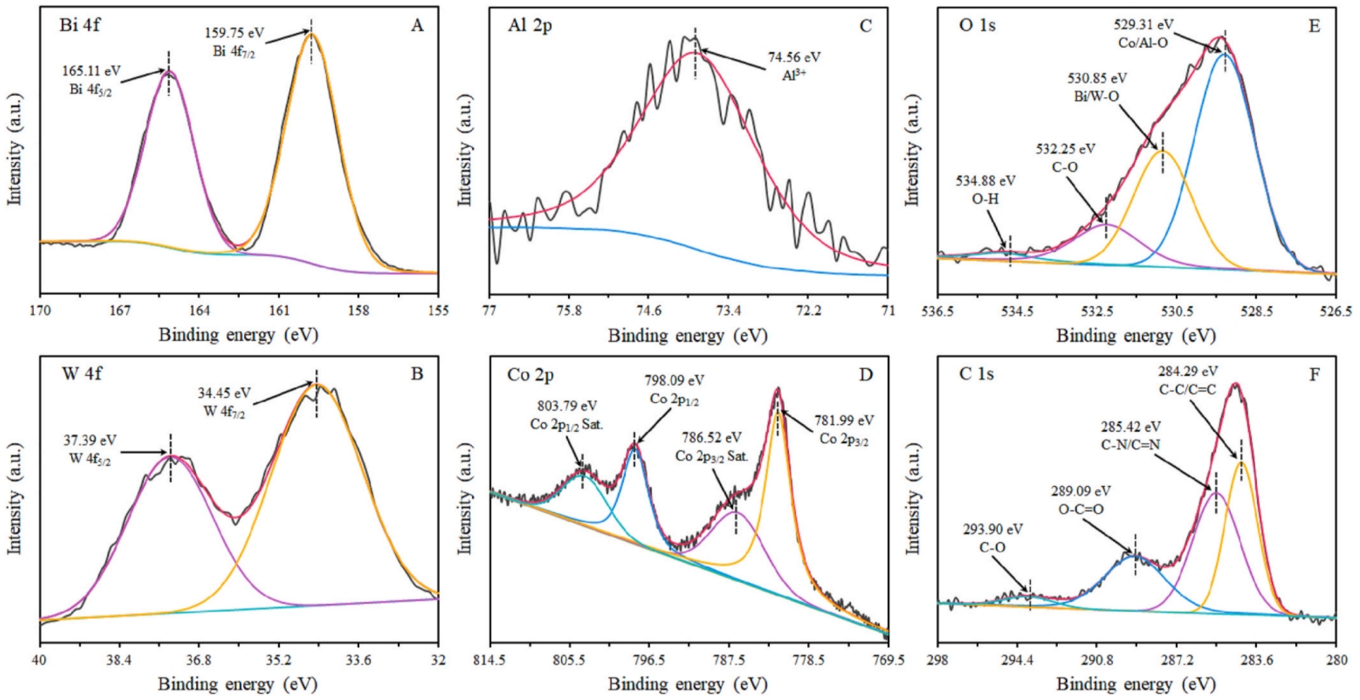

Fig. 3. XPS spectra of BWCA-20 sample.

and 530.85 eV were mainly assigned to oxygen in the sample lattice bonded with Co^{2+}, Al^{3+}, Bi^{3+} and W^{6+} (Jo et al., 2018; Das et al., 2019). Whereas the two additional peaks at 532.25 eV and 534.88 eV corresponded to C–O species and O–H groups of adsorbed water (Ma et al., 2016). As showed in Fig. 3F, the C 1s spectra of Bi_2WO_6/CoAl-LDHs was deconvoluted into four speaks at 284.29 eV (C–C/C=C), 285.42 eV (C–N/C=N), 289.09 eV (O–C=O) and 293.90 eV (C–O), in which the O–C=O peak was mainly due to the CO_3^{2-} between the CoAl-LDHs layers (Shao et al., 2018; Peng et al., 2017). As a result, the XPS results further affirmed the co-existence of CoAl-LDHs and Bi_2WO_6 in the Bi_2WO_6/CoAl-LDHs nanohybrid.

3.2. *Photo-fenton-like catalytic performance*

Firstly, the photocatalytic performance of the obtained catalysts was estimated by the photodegradation of OTC under visible light illumination. Compared with the Bi_2WO_6, the CoAl-LDHs and BWCA hybrids performed the higher adsorption performance for OTC in the dark

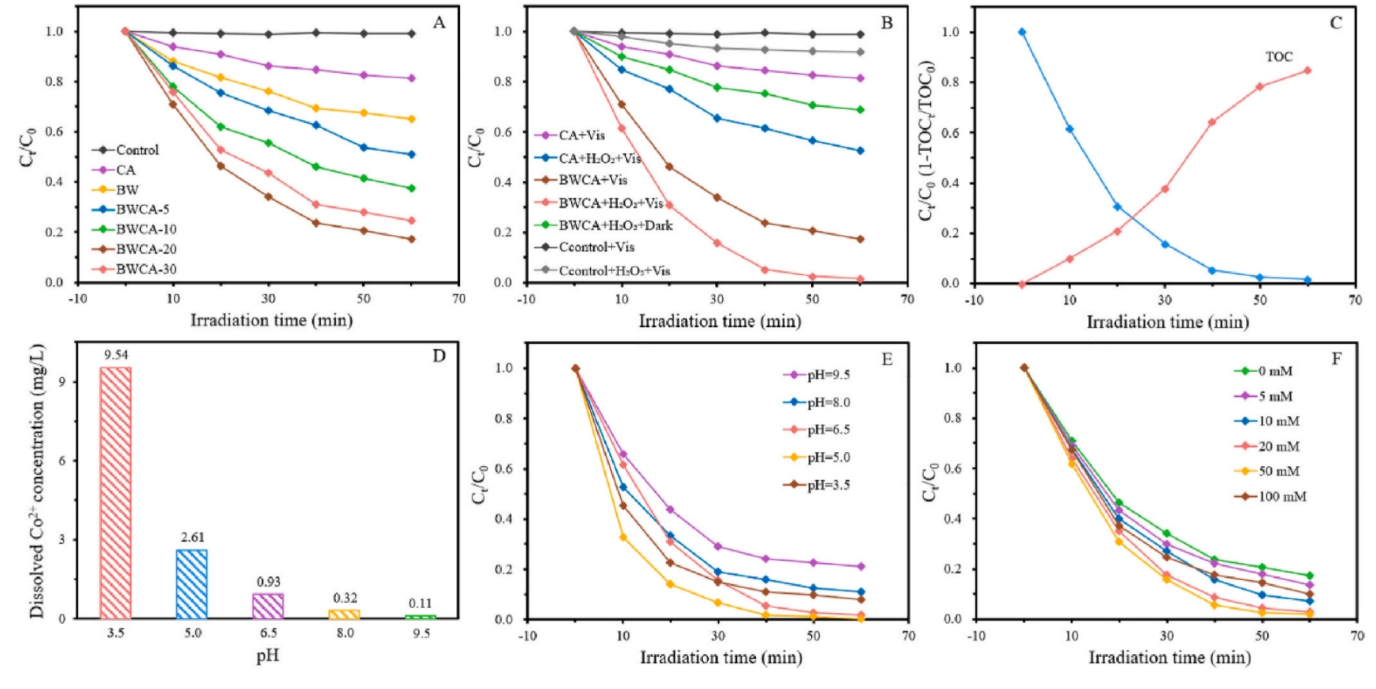

Fig. 4. The photocatalytic activity (A) and photo-Fenton-like catalytic activity (B) of as-prepared samples for OTC; TOC removal of OTC by BWCA-20 sample (C); Effect of pH value for the photo-Fenton-like catalytic of OTC by BWCA-20 sample (D); The amount of cobalt ions dissolved under different pH value (E); Effect of H_2O_2 concentration for the photo-Fenton-like catalytic of OTC by BWCA-20 sample (F).

(Fig. S2). After illumination, the photocatalytic efficiency of OTC by all catalysts was as follows: BWCA-20 (85.76%) > BWCA-30 (79.51%) > BWCA-10 (69.45%) > BWCA-5 (57.44%) > Bi_2WO_6 (41.75%) > CoAl-LDHs (32.88%) (Table S1, Fig. 4A). Evidently, all hybrids showed the better photocatalytic removal performance for OTC, which could be due to the heterojunction formation and the synergistic effect between Bi_2WO_6 and CoAl-LDHs, thus increasing the light absorption and restraining the recombination of photoexcited e^--h^+ pairs of BWCA hybrids. Meanwhile, the excessive Bi_2WO_6 would induce adverse effect on the photocatalytic performance of BWCA hybrids. Therefore, controlling the ratio of Bi_2WO_6 to CoAl-LDHs was very important to achieve optimized photocatalytic performance of the nanohybrid.

In consideration of the possible Fenton-like catalytic role of Co^{2+} (equations (3) and (4)), the photo-Fenton-like catalytic activity of the samples were futher studied in the presence of 0.05 M H_2O_2. As presented in Fig. 4B, the removal efficiency of OTC was increased obviously after adding the H_2O_2 in the catalytic system, and the maximum removal efficiency achieved 98.47% within 60 min. Meanwhile, the rate constant for OTC degradation in the mediation of H_2O_2 was about 2.38 times superior to that of the simple photocatalytic process (Table S1, Fig. S3). Furthermore, the mineralization performance of OTC by BWCA-20 was showed in Fig. 4C, obviously, the removal rate of OTC was slightly faster than that of mineralization rate, and the maximum mineralization efficiency reached 84.9% after 60 min of catalysis.

$$Co^{2+} + H_2O_2 \rightarrow Co^{3+} + \cdot OH + OH^- \tag{3}$$

$$Co^{3+} + H_2O_2 \rightarrow Co^{2+} + \cdot OOH + H^+ \tag{4}$$

For further exploring the role of Fenton-like catalytic process, the effect of pH and H_2O_2 concentration was studied. It is well known that the pH value plays a crucial role in the Fenton-like process, thus, a series of pH values (3.5, 5.0, 6.5, 8.0, 9.5) were adjusted by NaOH (0.1 M) or HNO_3 (0.1 M) to study the effect of initial pH in the photo-Fenton-like reaction. Obviously, the dissolved concentration of Co^{2+} increased with the decrease of pH (Fig. 4D). Meanwhile, the BWCA-20 composite possesses the higher photo-Fenton-like performance for OTC degradation when the pH value decreased to 5.0. This was because more ·OH would be produced in the Fenton reaction under acidic condition. At the same time, the cobalt ions on the catalyst surface would be slightly dissolved under acidic condition, which makes some reactions became homogeneous reaction. Generally, the homogeneous reaction rate is higher than the heterogeneous reaction rate, thus accelerating the reaction rate. But when the pH was 3.5, the photo-Fenton-like performance was declined (Fig. 4E), which could be because that the BWCA-20 nanohybrid was partially dissolved in the strongly acidic condition, thus leading to structural destruction of BWCA-20 and inhibiting their photocatalytic performance. Meanwhile, when pH went to 3.5, H_2O_2 could solvate protons to form oxonium ions ($H_3O_2{}^+$), which would enhance the stability of H_2O_2 and reduce its reactivity with cobalt ions (Cheng et al., 2016). In addition, the dissociated form of OTC was mainly H_3OTC^+, which has low reactivity with ·OH (Han et al., 2020). Furthermore, at the alkaline condition, the photo-Fenton-like performance was obviously inhibited (Fig. 4E), which could be due to (1) the cobalt ions were more likely to form complexes with OH^-, thus hindering the Fenton-like process; (2) the positively charged surface of CoAl-LDHs adsorbed too much negatively dissociated forms of OTC^{2-} and $HOTC^-$, thus disturbing the photocatalytic process (Han et al., 2020; Zhang et al., 2020b). In addition, the degradation of OTC at different H_2O_2 concentration was also displayed (Fig. 4F), clearly, the removal efficiency of OTC increased significantly along with the increase of H_2O_2 concentration from 5 to 50 mM, indicating that H_2O_2 concentrations were significantly related to the degradation of OTC. However, the increase in degradation rate of OTC was declined when H_2O_2 concentration up to 100 mM. This might be possibly result from the scavenging of ·OH by excessive H_2O_2 (equations (5) and (6)). For an excessive H_2O_2 loading, H_2O_2 could react with ·OH to generate ·OOH, leading to a reduction of catalytic performance (Cheng et al., 2019).

$$\cdot OH + H_2O_2 \rightarrow H_2O + \cdot OOH \tag{5}$$

$$\cdot OH + \cdot OOH \rightarrow H_2O + O_2 \tag{6}$$

The stability of catalysts performed important influence on their practical application, thus the cyclic photo-Fenton-like catalytic experiments of OTC by BWCA-20 composite were carried out (Fig. 5A). Evidently, the BWCA-20 nanohybrid retained almost 88.74% of its original activity for OTC decomposition even after four continuous cycles, indicating the BWCA nanohybrids could be a stable catalyst. A slight decline of removal efficiency should be due to the inevitable loss of the catalyst in the cyclic and the adsorption of some refractory intermediate products on the active site of catalyst (Jo and Tonda, 2019). The phase and structural stabilities of the BWCA-20 nanohybrid were further investigated by XRD analyses. As shown in Fig. 5B, the chemical structure of BWCA-20 nanohybrid had no noticeable variation during the prolonged degradation reactions. Furthermore, the Co^{2+} leaching amount was showed in Fig. 5C, and the Co^{2+} leaching meets China's Environmental Quality Standards for Surface Water (<1.0 mg/L) (GB25467-2010). Therefore, the prepared Bi_2WO_6/CoAl-LDHs nanohybrid was promising catalyst for environmental protection due to the prominent catalytic performance and high stability.

3.3. *Optical-electrical characteristics analysis*

The optical-electrical characteristics are crucial to the activity of photocatalysts, herein, the UV–vis DRS, photoelectrochemical and photoluminescence tests were introduced. As depicted in Fig. 6A, the UV–vis DRS spectrum showed the light response property of the samples, apparently, the Bi_2WO_6 was sensitively responsive to UV-light but less to visible light, only exhibited the absorption edge at around 450 nm (Wang et al., 2018c). The pure CoAl-LDHs also displayed an obvious absorption for UV, while had low absorption peak in the visible region, although there was a broad band in the visible region centered around 500 nm (due to d-d transitions of octahedral Co^{2+} within the CoAl-LDHs layer) (Kumar et al., 2017; Jo and Tonda, 2019). As for the Bi_2WO_6/CoAl-LDHs composite, the absorption of visible light increased in some extent, which be conducive to improve the photocatalytic performance of composite. Besides, the E_g of the pure Bi_2WO_6 and CoAl-LDHs was assessed from the Tauc's equation: $\alpha h\nu = A (h\nu - E_g)^{n/2}$ (Shao et al., 2021b). According to the calculation, the E_g of Bi_2WO_6 and CoAl-LDHs was about 2.72 eV and 2.33 eV, respectively (Fig. 6A). Meanwhile, the potentials of conduction band (CB) and valence band (VB) of Bi_2WO_6 and CoAl-LDHs could be determined based on the following equations: $E_{VB} = X\text{-}E^e + 0.5E_g$, $E_{CB} = E_{VB}\text{-}E_g$ (Xia et al., 2020a). The calculated VB of Bi_2WO_6 and CoAl-LDHs were 3.22 eV and 1.70 eV, respectively, and the calculated CB was 0.50 eV and −0.63 eV, respectively.

Photoelectrochemical performance was deemed as the credible criterion for evaluating the photocurrent responses and the photogenerated charges separation of the photocatalyst. Fig. 6B showed the photocurrent intensity of the samples under visible light irradiation. Obviously, both of Bi_2WO_6 and CoAl-LDHs samples performed a lower photocurrent intensity than that of Bi_2WO_6/CoAl-LDHs-20. Additionally, the charge transfer rate was assessed based on the arc radius in the EIS, generally, the smaller arc in the EIS represents the faster charge migration (Shao et al., 2018). As presented in Fig. 6C, clearly, the Bi_2WO_6/CoAl-LDHs-20 nanohybrid would perform the fastest charge transfer due to the smallest arc in the EIS. The photocurrent and EIS results suggested that the existence of heterojunction of Bi_2WO_6/CoAl-LDHs-20 nanohybrid, which was benefit for the electron transfer process, thus effectively decreased the recombination of photoexcited e^--h^+ pairs and promoted the photocatalytic activity of photocatalysts. Further understanding the transfer behavior of the photoinduced carriers of obtained samples, PL detection was implemented (Fig. 6D). The emission peak of Bi_2WO_6/CoAl-LDHs nanohybrid at 620 nm was lower

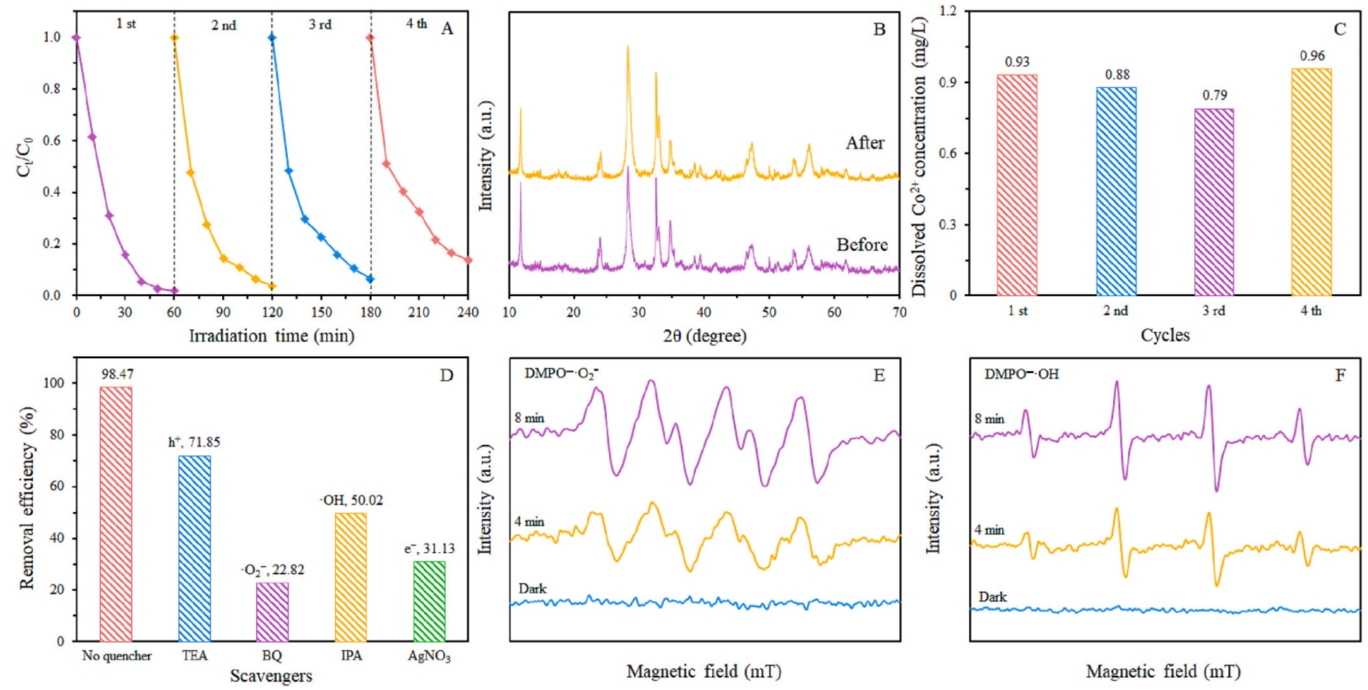

Fig. 5. The cyclic photo-Fenton-like catalytic experiments for the degradation of OTC (A); The XRD pattern of the BWCA-20 sample after 4th run cycles (B); The cobalt ions leaching amount during the cyclic experiments (C); Trapping experiments of radical species during the photo-Fenton-like catalytic of OTC by BWCA-20 sample (D); EPR spectra of radical adducts trapped by DMPO (•O_2^- (E) and •OH (F)) in BWCA-20 sample dispersion in the dark and under visible light illumination.

than that of single material, implying the recombination of photoexcited e^--h^+ pairs was highly suppressed due to the interfacial charge transfer between CoAl-LDHs and Bi_2WO_6 (Wu et al., 2018).

3.4. Theoretical calculations

Some important electronic and optical properties of the above catalysts were further investigated by DFT calculation (The details are displayed in the SI). The geometries and lattice parameters of Bi_2WO_6, CoAl-LDHs and Bi_2WO_6/CoAl-LDHs were displayed in Fig. S4A and Table S2. Firstly, the electronic properties of band structures were displayed in Fig. S5, the results showed that the calculated E_g values (2.845 and 2.248 eV for Bi_2WO_6 and CoAl-LDHs, respectively) was very close to the tested E_g values and previous theoretical calculation results (Xu et al., 2015), and the E_g value of Bi_2WO_6/CoAl-LDHs was difficulty be revealed due to the overlap of their band structures (Liang et al., 2021b). Meanwhile, the band structure further indicated that Bi_2WO_6 and CoAl-LDHs were both indirect band-gap semiconductors. Furthermore, the effective mass of electron for Bi_2WO_6, CoAl-LDHs and Bi_2WO_6/CoAl-LDHs could be calculated based on their band structure, and the values were 0.197, 0.428 and 0.142, respectively. Obviously, the Bi_2WO_6/CoAl-LDHs possessed the smaller effective mass of electron, suggesting the higher mobility of electron. Thus, the separation of photoinduced e^--h^+ pairs and photocatalytic activity would be enhanced in the Bi_2WO_6/CoAl-LDHs systems (Zhang et al., 2018). Secondly, the orbital states of electrons in different samples had been revealed by their density of states (Fig. S5). Compared with Bi_2WO_6 and CoAl-LDHs, the Bi_2WO_6/CoAl-LDHs heterojunction performed the higher electron intensity, which should be attributed to the hybridization of different electron orbitals and the efficient electron transfer between Bi_2WO_6 and CoAl-LDHs. Simultaneously, the occurrence of electron transfer between Bi_2WO_6 and CoAl-LDHs could be further confirmed by the charge density difference due to the uneven charge distribution at the interface (Fig. S4A). In addition, the work function (WF) of material also plays a key role in the study of interfacial charge transfer, and could determine the transfer direction of the photogenerated electrons between the different photocatalytic materials (Liu et al., 2020b). As displayed in Fig. 7A–C, the calculated WF of Bi_2WO_6, CoAl-LDHs and Bi_2WO_6/CoAl-LDHs was 5.89 eV, 5.28 eV and 5.45 eV, respectively. Obviously, the CoAl-LDHs performed a lower WF than that of Bi_2WO_6, suggesting the charges could readily flow from CoAl-LDHs to Bi_2WO_6 once contacted (Shao et al., 2020a, 2021b). Furthermore, the Fermi level (E_F) can be converted by following equations (7)–(9) (Cao et al., 2018). Thus, the E_F of Bi_2WO_6, CoAl-LDHs and Bi_2WO_6/CoAl-LDHs was 0.977 eV, 0.367 eV and 0.537 eV, respectively.

$$E_F(\text{vs VAC}) = E_{VAC} - \text{WF} \tag{7}$$

$$E_F(\text{vs NHE, pH} = 0) = -4.5 – E_F(\text{vs VAC}) \tag{8}$$

$$E_F(\text{vs NHE, pH} = 7) = E_F(\text{vs NHE, pH} = 0) – 0.059\text{pH} \tag{9}$$

Furthermore, the optical properties of absorption coefficient and loss function of the samples were calculated. As presented in Fig. 7D, compared with the CoAl-LDHs, the visible light absorption efficiency of Bi_2WO_6/CoAl-LDHs was significantly improved, the result was consistent with that of UV–vis DRS. The energy loss function corresponding to the energy region, in which the electrons were not typically restricted to their lattice sites and exhibited plasma oscillations upon light irradiation (Rizwan et al., 2019). Meanwhile, the energy loss function could reflect the energy losses by a rapid electron penetrating across the medium. As shown in Fig. 7E, the CoAl-LDHs performed a well-defined abrupt loss peak, however, no obvious loss peak was observed in the Bi_2WO_6/CoAl-LDHs system. The energy loss function spectra indicated that the heterojunction system could significantly reduce the energy loss of electrons during photocatalytic process, then improving the photocatalytic performance of Bi_2WO_6/CoAl-LDHs hybrids. The theoretical results showed that the introduction of Bi_2WO_6 could improve the electronic and optical properties of CoAl-LDHs, which would increase the response to VSL, accelerate charge transfer, reduce e^--h^+ pairs recombination, then increasing the photocatalytic performance of the material, the results were consistent with the experimental results.

In addition to those, the adsorption and dissociation behavior of

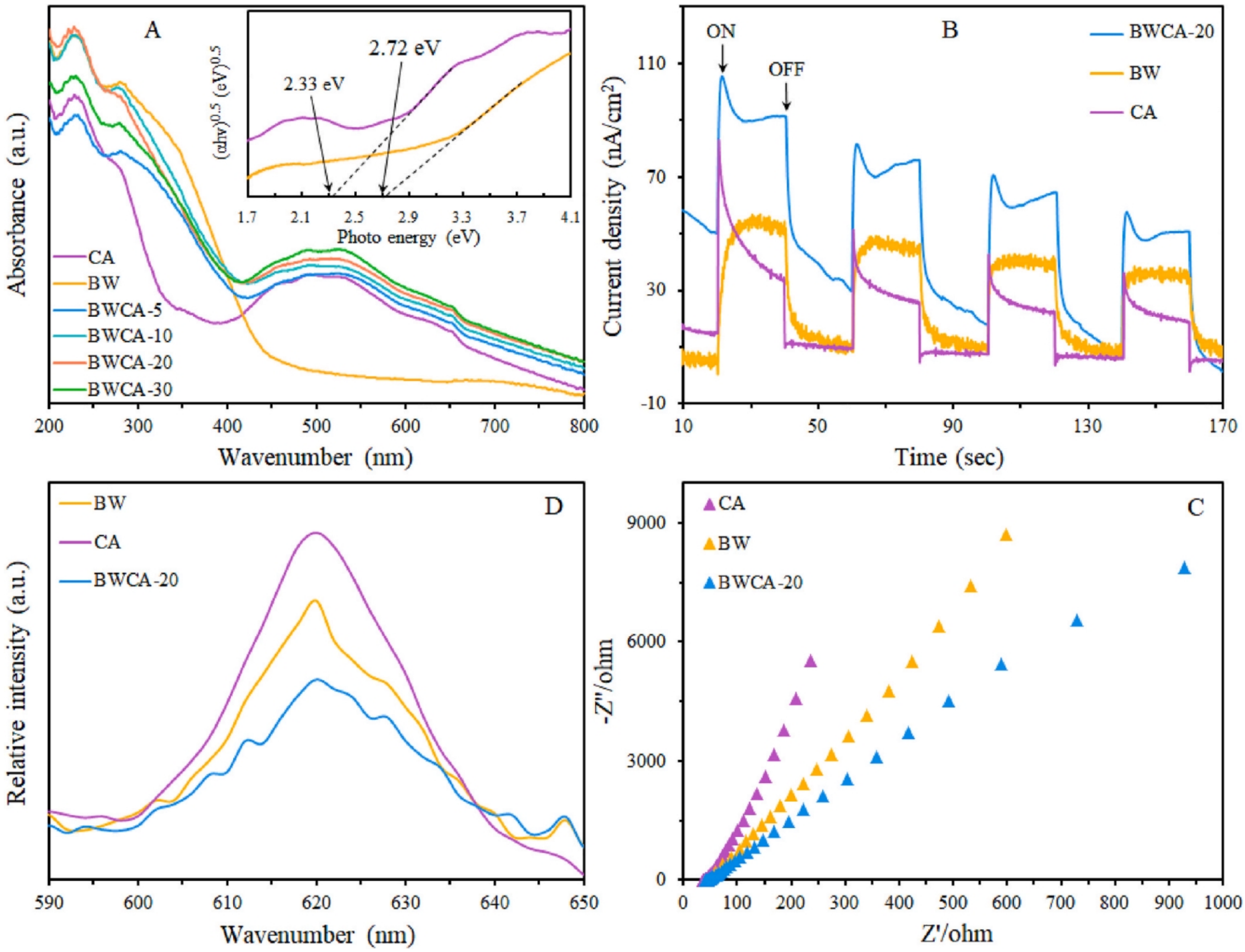

Fig. 6. UV–vis spectrum, band gap energies (A), transient photocurrent (B), EIS (C) and PL (D) spectra of the as-prepared samples.

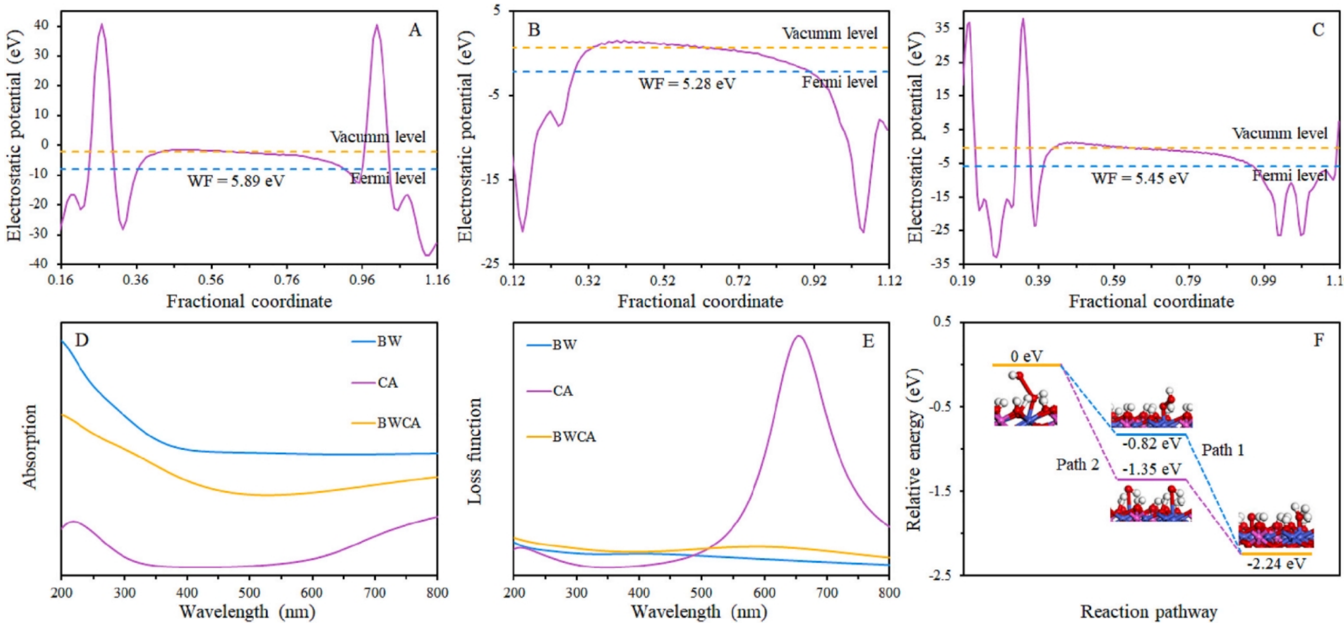

Fig. 7. The work function of Bi_2WO_6 (A), CoAl-LDHs (B) and Bi_2WO_6/CoAl-LDHs (C); The absorption coefficient (D) and loss function (E) of the above models; Relative energy change diagram of the decomposition process of H_2O_2 on the CoAl-LDHs surface (F).

H_2O_2 on the surface of CoAl-LDHs were also studied by using DFT calculation. Firstly, the model of H_2O_2 adsorbed on CoAl-LDHs surface was constructed, the possible adsorption sites (Top, Hcp and Fcc) and orientations (parallel and vertical) of H_2O_2 were considered (Fig. S4B), and the two stable adsorption configurations (Hcp-Al, parallel; Hcp-Co, vertical) were obtained by geometry optimization (Fig. S4C). As listed in Table S3, the adsorption energy was −28.92 eV and −28.44 eV for Hcp-Al and Hcp-Co sites, respectively. Meanwhile, a negative value of adsorption energy represented the exothermic adsorption (Song et al., 2017; Li et al., 2020). Furthermore, the O–O bond had more obvious variation than O–H bond, which could signify the decomposition of H_2O_2 on the surface of CoAl-LDHs was O–O band breaking firstly (Guo et al., 2019). Previous studies indicated that the H_2O_2 usually has two decomposition pathways (equations 10 and 11, IS, TS and FS represents initial, transition and final states, respectively) (Guo et al., 2019; Song et al., 2018), and the decomposition behavior of H_2O_2 on CoAl-LDHs surface was further simulated.

$$H_2O_2(IS) \rightarrow \ OOH \ + \ H \ (TS1) \rightarrow \ H_2O \ + \ O \ (FS) \tag{10}$$

$$H_2O_2(IS) \rightarrow 2OH \ (TS2) \rightarrow \ H_2O \ + \ O \ (FS) \tag{11}$$

As displayed in Fig. 7F, the first step was total energy of H_2O_2 adsorbed on CoAl-LDHs, and assuming it as the 0 eV. The second step was total energy of OOH and H or double OH adsorbed on CoAl-LDHs. The last step was the total energy of H_2O and O atom adsorbed on CoAl-LDHs. Obviously, both reaction energy were negative value, indicating the dissociation was an exothermic process. Meanwhile, compared to the path 1 ($H_2O_2 \rightarrow OOH + H$), the energy of path 2 ($H_2O_2 \rightarrow 2OH$) was decreased more, which implied the O–O bond breaks more than O–H bond, and the decomposition of H_2O_2 on CoAl-LDHs surface was more follow the path 2 (Guo et al., 2019).

3.5. *Mechanism of the photo-Fenton-like catalytic system*

For exploring the catalytic mechanism, the reactive active species in the catalytic system had been investigated by trapping experiments. As indicated in Fig. 5D, the degradation of OTC was inhibited in different extent in the presence of different scavengers. The degradation efficiencies were decreased to 22.82%, 50.02%, 71.85% and 31.13% in the presence of *p*-benzoquinone (BQ, $\cdot O_2^-$ scavenger), isopropanol (IPA, ·OH scavenger), triethanolamine (TEA, h^+ scavenger) and $AgNO_3$ (e^- scavenger), respectively. It was demonstrated that the $\cdot O_2^-$ and ·OH played the more critical role in the photo-Fenton-like catalytic degradation of OTC than that of h^+ (Wei et al., 2019). Meanwhile, the e^- was of great significance to this catalytic system, which could play a pivotal role in the production of reactive active species in the catalytic system. To further verify the generation of these radicals in photocatalytic process, the ESR spin-trap tests were carried out. As shown in Fig. 5E, the peak intensity of DMPO-$\cdot O_2^-$ and DMPO-·OH was negligible in the dark, after illumination, both of their peaks increased obviously, indicating the produce of the $\cdot O_2^-$ and ·OH radicals in the photocatalytic process.

Based on the above experimental and theoretical results, the photo-Fenton-like catalytic mechanism of Bi_2WO_6/CoAl-LDHs nanohybrid for pollutant degradation was proposed in Fig. 8. As above results, the potentials of CB and VB were 0.50 eV and 3.22 eV for Bi_2WO_6, -0.63 eV and 1.70 eV for CoAl-LDHs, respectively. Before contact, the Fermi level (E_F) was the chemical potential of thermodynamic equilibrium, and the above calculation indicated that the E_F of Bi_2WO_6 and CoAl-LDHs was 0.977 eV and 0.367 eV, respectively. However, when Bi_2WO_6 and CoAl-LDHs come into contact, the difference of WF could drive the electrons spontaneously diffuse from CoAl-LDHs to Bi_2WO_6, creating an electron accumulation layer and an electron depletion layer near the interface in Bi_2WO_6 and CoAl-LDHs, respectively, consequently, the Bi_2WO_6 and CoAl-LDHs possess negative and positive charges, respectively. Simultaneously, an internal electric field originating from CoAl-LDHs to Bi_2WO_6 was appeared, which would accelerate the photogenerated electrons transfer from Bi_2WO_6 to CoAl-LDHs (Zhang et al., 2020c). Meanwhile, after contact, the E_F would be aligned to the same level, thus leading to an upward and downward shift in the E_F of Bi_2WO_6 to CoAl-LDHs, respectively. The band bending urged the recombination of the photoinduced electrons in the CB of Bi_2WO_6 and holes in the VB of CoAl-LDHs at the interface region, just like water flows downhill.

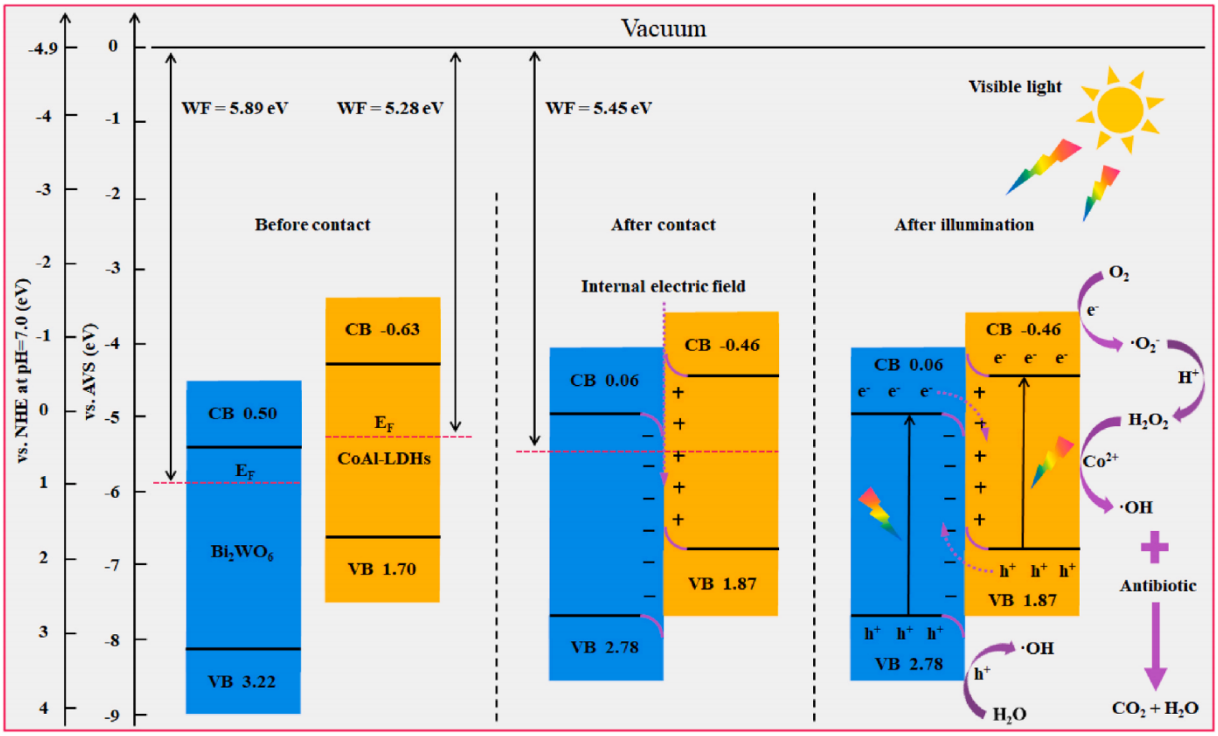

Fig. 8. Schematic diagram for possible charge separation and photo-Fenton-like catalytic mechanism of S-scheme heterojunction of Bi_2WO_6/CoAl-LDHs.

Furthermore, the coulombic attraction would also impel the recombination between the electrons in the CB of Bi_2WO_6 and the holes in the VB of CoAl-LDHs. As a result, the useless electrons and holes are annihilated via recombination, while the efficient photoinduced electrons in the CB of CoAl-LDHs and the holes in the VB of Bi_2WO_6 are reserved, this charge-transfer route was highly follow the S-scheme heterojunction (Xu et al., 2020). The accumulated electrons in the CB of CoAl-LDHs could reduce O_2 to generate $\cdot O_2^-$ ($O_2/\cdot O_2^-$, -0.046 eV) (equation (15)), while the resident holes in the VB of Bi_2WO_6 would oxide H_2O into $\cdot OH$ ($H_2O/\cdot OH$, 2.72 eV) (equation (16)). Meanwhile, the presence of Co^{2+} in the CoAl-LDHs will activate the Fenton-like reaction by the added or generated H_2O_2 (equations 21 and 22). Ultimately, the antibiotic would be degraded and mineralized to CO_2, H_2O or others by the formed strong oxidized active species (h^+, $\cdot O_2^-$, $\cdot OH$) during the photocatalysis and Fenton-like catalysis processes (equation (23)). The mainly possible reactions in the catalytic system are listed as follows:

$$Bi_2WO_6 + \ \mathrm{VSL} \ \rightarrow Bi_2WO_6(\mathrm{e}^- - \mathrm{h}^+) \tag{12}$$

$$\mathrm{CoAl-LDHs} \ + \ \mathrm{VSL} \ \rightarrow \ \mathrm{CoAl-LDHs} \ (\mathrm{e}^- - \mathrm{h}^+) \tag{13}$$

$$Bi_2WO_6(\mathrm{e}^-) + \ \mathrm{CoAl-LDHs} \ (\mathrm{h}^+) \rightarrow Recombination \tag{14}$$

$$\mathrm{CoAl-LDHs} \ (\mathrm{e}^-) + \ \mathrm{O_2} \rightarrow \cdot \mathrm{O_2^-} \tag{15}$$

$$Bi_2WO_6(\mathrm{h}^+) + \ \mathrm{H_2O} \ \rightarrow \cdot \mathrm{OH} \tag{16}$$

$$\cdot \mathrm{O_2^-} + \ \mathrm{H}^+ \rightarrow \cdot \mathrm{OOH} \tag{17}$$

$$\cdot \mathrm{OOH} \ + \ \mathrm{H}^+ + \ \mathrm{e}^- \rightarrow \ \mathrm{H_2O_2} \tag{18}$$

$$\mathrm{O_2} + 2\mathrm{H}^+ + 2\mathrm{e}^- \rightarrow \ \mathrm{H_2O_2} \tag{19}$$

$$\mathrm{H_2O_2} + \ \mathrm{e}^- \rightarrow \cdot \mathrm{OH} \ + \ \mathrm{OH}^- \tag{20}$$

$$Co^{2+} + \ \mathrm{H_2O_2} \rightarrow Co^{3+} + \cdot \mathrm{OH} \ + \ \mathrm{OH}^- \tag{21}$$

$$Co^{3+} + H_2O_2 \rightarrow Co^{2+} + \cdot OOH + H^+ \tag{22}$$

$$\mathrm{h}^+ + \cdot \mathrm{O_2^-} + \cdot \mathrm{OH} \ + \ \mathrm{OTC} \ \rightarrow \ \mathrm{Degradation \ \ products} \tag{23}$$

4. Conclusions

In summary, the hortensia-like Bi_2WO_6/CoAl-LDHs nanohybrids were synthesized via hydrothermal process. The photo-Fenton-like catalytic tests manifested that the maximum removal efficiency of OTC reached 98.47% by the optimized Bi_2WO_6/CoAl-LDHs-20 sample, which was obviously higher than that of the single photocatalytic process. Variety characterization techniques and DFT calculation indicated that the high-efficiency photo-Fenton-like catalytic performance of Bi_2WO_6/CoAl-LDHs was due to the synergistic effect of the Fenton-like process of cobalt ions in CoAl-LDHs, an internal electric field and the S-scheme heterojunction form between Bi_2WO_6 and CoAl-LDHs. This study showed that the combined catalytic system of photocatalysis and Fenton-like catalysis would perform the greater application prospects in environmental remediation.

Credit author statement

Binbin Shao: Conceptualization, Methodology, Software, Investigation, Validation, Writing – original draft, Funding acquisition. Zhifeng Liu: Conceptualization, Resources, Project administration, Funding acquisition. Lin Tang: Resources, Project administration, Funding acquisition. Qinghua Liang: Validation, Writing – review & editing. Qingyun He: Investigation, Data curation. Ting Wu: Investigation, Data curation. Yuan Pan: Data curation. Min Cheng: Validation, Writing – review & editing. Yang Liu: Validation, Writing – review & editing. Xiaofei Tan: Writing – review & editing. Jing Tang: Writing – review & editing. Hou Wang: Writing – review & editing. Haopeng Feng: Writing – review & editing. Shehua Tong: Writing – review & editing.

Declaration of competing interest

The authors declare that they have no known competing financial interests or personal relationships that could have appeared to influence the work reported in this paper.

Acknowledgments

The study was financially supported by the Program for Changjiang Scholars and Innovative Research Team in University (IRT-13R17), the National Natural Science Foundation of China (52100181, 51979103, 51679085, 51521006, 51508177), the Project funded by China Postdoctoral Science Foundation (2021T140192, 2021M690054), the Funds of Hunan Science and Technology Innovation Project (2018RS3115, 2020RC5012). The authors also gratefully acknowledge the National Supercomputing Center in Changsha for providing the computing resources.

Appendix A. Supplementary data

Supplementary data to this article can be found online at https://doi.org/10.1016/j.chemosphere.2021.133001.

References

Ahmad, R., Kumar, R., 2010. J. Environ. Manag. 91, 1032–1038.

Cao, S., Shen, B., Tong, T., Fu, J., Yu, J., 2018. Adv. Funct. Mater. 28, 1800136.

Chen, J., He, Z., Li, G., An, T., Shi, H., Li, Y., 2017. Appl. Catal., B 209, 146–154.

Chen, Y., Jing, C., Zhang, X., Jiang, D., Liu, X., Dong, B., Feng, L., Li, S., Zhang, Y., 2019. J. Colloid Interface Sci. 548, 100–109.

Cheng, M., Zeng, G., Huang, D., Lai, C., Xu, P., Zhang, C., Liu, Y., 2016. Chem. Eng. J. 284, 582–598.

Cheng, M., Zeng, G., Huang, D., Lai, C., Liu, Y., Zhang, C., Wan, J., Hu, L., Zhou, C., Xiong, W., 2018. Water Res. 138, 7–18.

Cheng, M., Liu, Y., Huang, D., Lai, C., Zeng, G., Huang, J., Liu, Z., Zhang, C., Zhou, C., Qin, L., Xiong, W., Yi, H., Yang, Y., 2019. Chem. Eng. J. 362, 865–876.

Das, S., Patnaik, S., Parida, K.M., 2019. Inorg. Chem. Front. 6, 94–109.

Duan, M., Jiang, L., Zeng, G., Wang, D., Tang, W., Liang, J., Wang, H., He, D., Liu, Z., Tang, L., 2020. Appl. Mater. Today 19, 100564.

Guo, Y., Hu, R., Zhou, X., Yu, J., Wang, L., 2019. Appl. Surf. Sci. 479, 989–996.

Guo, X.X., Hu, T.T., Meng, B., Sun, Y., Han, Y.F., 2020. Appl. Catal., B 260, 118157.

Han, C.H., Park, H.D., Kim, S.B., Yargeau, V., Choi, J.W., Lee, S.H., Park, J.A., 2020. Water Res. 172, 115514.

Hu, J., Chen, D., Mo, Z., Li, N., Xu, Q., Li, H., He, J., Xu, H., Lu, J., 2019. Angew. Chem. Int. Ed. 58, 2073–2077.

Huang, J., Liu, X., Liu, Z., Zhong, H., Shao, B., Liang, Q., Liu, Y., Zhang, W., He, Q., 2020. Chem. Eng. J. 404.

Islam, D.A., Barman, K., Jasimuddin, S., Acharya, H., 2019. Nanoscale 11, 7560–7566.

Jo, W.K., Tonda, S., 2019. J. Hazard Mater. 368, 778–787.

Jo, W.K., Kumar, S., Eslava, S., Tonda, S., 2018. Appl. Catal., B 239, 586–598.

Kumar, S., Isaacs, M.A., Trofimovaite, R., Durndell, L., Parlett, C.M.A., Douthwaite, R.E., Coulson, B., Cockett, M.C.R., Wilson, K., Lee, A.F., 2017. Appl. Catal., B 209, 394–404.

Li, H.l., Dong, F.Q., Bian, L., Huo, T.T., He, X.C., Zheng, F., Lv, Z.Z., Jiang, L.M., Li, B., 2020. Colloid. Surface. 125777.

Liang, Q., Shao, B., Tong, S., Liu, Z., Tang, L., Liu, Y., Cheng, M., He, Q., Wu, T., Pan, Y., 2020. Chem. Eng. J. 405.

Liang, C., Niu, H.Y., Guo, H., Niu, C.G., Yang, Y.Y., Liu, H.Y., Tang, W.W., Feng, H.P., 2021a. Chem. Eng. J. 406, 126868.

Liang, Q., Liu, X., Wang, J., Liu, Y., Liu, Z., Tang, L., Shao, B., Zhang, W., Gong, S., Cheng, M., He, Q., Feng, C., 2021b. J. Hazard Mater. 401, 123355.

Liu, Z., Jiang, Y., Liu, X., Zeng, G., Shao, B., Liu, Y., Liu, Y., Zhang, W., Zhang, W., Yan, M., He, X., 2019. Compos. B Eng. 173, 106918.

Liu, Y., Huang, D., Cheng, M., Liu, Z., Lai, C., Zhang, C., Zhou, C., Xiong, W., Qin, L., Shao, B., Liang, Q., 2020a. Coord. Chem. Rev. 409, 213220.

Liu, Y., Li, Y.H., Li, X., Zhang, Q., Yu, H., Peng, X., Peng, F., 2020b. ACS Nano 14, 14181–14189.

Lu, P., Lin, K., Gan, J., 2020. Water Res. 183, 116105.

Ma, D., Wu, J., Gao, M., Xin, Y., Ma, T., Sun, Y., 2016. Chem. Eng. J. 290, 136–146.

Pan, Y., Liu, X., Zhang, W., Liu, Z., Zeng, G., Shao, B., Liang, Q., He, Q., Yuan, X., Huang, D., Chen, M., 2020. Appl. Catal., B 265, 118579.

Peng, W., Li, H., Song, S., 2017. ACS Appl. Mater. Interfaces 9, 5204–5212.

Peng, Z., Liu, X., Zhang, W., Zeng, Z., Liu, Z., Zhang, C., Liu, Y., Shao, B., Liang, Q., Tang, W., Yuan, X., 2020. Environ. Int. 134, 105298.
Ren, Y., Shi, M., Zhang, W., Dionysiou, D.D., Lu, J., Shan, C., Zhang, Y., Lv, L., Pan, B., 2020. Environ. Sci. Technol. 54, 5258–5267.
Rizwan, M., Ali, A., Usman, Z., Khalid, N.R., Jin, H.B., Cao, C.B., 2019. Physica B 552, 52–57.
Shao, B., Liu, Z., Zhong, H., Zeng, G., Liu, G., Yu, M., Liu, Y., Yang, X., Li, Z., Fang, Z., Zhang, J., Zhao, C., 2017. Microbiol. Res. 200, 33–44.
Shao, B., Liu, Z., Zeng, G., Wu, Z., Liu, Y., Cheng, M., Chen, M., Liu, Y., Zhang, W., Feng, H., 2018. ACS Sustain. Chem. Eng. 6, 16424–16436.
Shao, B., Liu, Z., Zeng, G., Liu, Y., Yang, X., Zhou, C., Chen, M., Liu, Y., Jiang, Y., Yan, M., 2019a. J. Hazard Mater. 362, 318–326.
Shao, B., Liu, X., Liu, Z., Zeng, G., Liang, Q., Liang, C., Cheng, Y., Zhang, W., Liu, Y., Gong, S., 2019b. Chem. Eng. J. 368, 730–745.
Shao, B., Liu, X., Liu, Z., Zeng, G., Zhang, W., Liang, Q., Liu, Y., He, Q., Yuan, X., Wang, D., Luo, S., Gong, S., 2019c. Chem. Eng. J. 374, 479–493.
Shao, B., Wang, J., Liu, Z., Zeng, G., Tang, L., Liang, Q., He, Q., Wu, T., Liu, Y., Yuan, X., 2020a. J. Mater. Chem. 8, 5171–5185.
Shao, B., Liu, Z., Zeng, G., Wang, H., Liang, Q., He, Q., Cheng, M., Zhou, C., Jiang, L., Song, B., 2020b. J. Mater. Chem. 8, 7508–7535.
Shao, B., Liu, Z., Zeng, G., Liu, Y., Liang, Q., He, Q., Wu, T., Pan, Y., Huang, J., Peng, Z., Luo, S., Liang, C., Liu, X., Tong, S., Liang, J., 2021a. Appl. Catal., B 286, 119867.
Shao, B., Liu, Z., Zeng, G., Liu, Y., Liang, Q., He, Q., Wu, T., Pan, Y., Huang, J., Peng, Z., Luo, S., Liang, C., Liu, X., Tong, S., Liang, J., 2021b. Appl. Catal., B 286, 119867.
Song, Z., Wang, B., Yu, J., Ma, C., Zhou, C., Chen, T., Yan, Q., Wang, K., Sun, L., 2017. Appl. Surf. Sci. 413, 292–301.
Song, Z., Wang, B., Yu, J., Ma, C., Chen, T., Yang, W., Liu, S., Sun, L., 2018. Chem. Eng. J. 354, 517–524.
Tao, J., Yu, X., Liu, Q., Liu, G., Tang, H., 2021. J. Colloid Interface Sci. 585, 470–479.
Wang, J., Tang, L., Zeng, G., Deng, Y., Liu, Y., Wang, L., Zhou, Y., Guo, Z., Wang, J., Zhang, C., 2017. Appl. Catal., B 209, 285–294.
Wang, Q., Chen, L., Guan, S., Zhang, X., Wang, B., Cao, X., Yu, Z., He, Y., Evans, D.G., Feng, J., Li, D., 2018a. ACS Catal. 8, 3104–3115.
Wang, H., Jing, M., Wu, Y., Chen, W., Ran, Y., 2018b. J. Hazard Mater. 353, 53–61.
Wang, J., Tang, L., Zeng, G., Deng, Y., Dong, H., Liu, Y., Wang, L., Peng, B., Zhang, C., Chen, F., 2018c. Appl. Catal., B 222, 115–123.
Wang, J., Liang, H., Zhang, C., Jin, B., Men, Y., 2019. Appl. Catal., B 256, 117874.
Wei, P., Qin, D., Chen, J., Li, Y., Wen, M., Ji, Y., Li, G., An, T., 2019. Environ. Sci. Nano 6, 959–969.
Wu, Y., Wang, H., Sun, Y., Xiao, T., Tu, W., Yuan, X., Zeng, G., Li, S., Chew, J.W., 2018. Appl. Catal., B 227, 530–540.
Wu, S., Liu, H., Yang, C., Li, X., Lin, Y., Yin, K., Sun, J., Teng, Q., Du, C., Zhong, Y., 2020a. Chem. Eng. J. 392, 123683.
Wu, T., Liu, X., Liu, Y., Cheng, M., Liu, Z., Zeng, G., Shao, B., Liang, Q., Zhang, W., He, Q., Zhang, W., 2020b. Coord. Chem. Rev. 403, 213097.
Xia, S., Zhang, G., Meng, Y., Yang, C., Ni, Z., Hu, J., 2020a. Appl. Catal., B 278, 119266.
Xia, P., Cao, S., Zhu, B., Liu, M., Shi, M., Yu, J., Zhang, Y., 2020b. Angew. Chem. Int. Ed. 59, 5218–5225.
Xu, S.M., Pan, T., Dou, Y.B., Yan, H., Zhang, S.T., Ning, F.Y., Shi, W.Y., Wei, M., 2015. J. Phys. Chem. C 119, 18823–18834.
Xu, Q., Zhang, L., Cheng, B., Fan, J., Yu, J., 2020. Inside Chem. 6, 1543–1559.
Yang, Z.Z., Zhang, C., Zeng, G.M., Tan, X.F., Wang, H., Huang, D.l., Yang, K.H., Wei, J.J., Ma, C., Nie, K., 2020. J. Mater. Chem. 8, 4141–4173.
Zhang, L., Zhang, X., Shen, L., Gao, B., Hao, L., Lu, X., Zhang, F., Ding, B., Yuan, C., 2012. J. Power Sources 199, 395–401.
Zhang, Y., Du, D., Li, X., Sun, H., Li, L., Bai, P., Xing, W., Xue, Q., Yan, Z., 2017. ACS Appl. Mater. Interfaces 9, 31699–31709.
Zhang, Y.C., Li, Z., Zhang, L., Pan, L., Zhang, X., Wang, L., Fazal e, A., Zou, J.J., 2018. Appl. Catal., B 224, 101–108.
Zhang, Q., Jiang, L., Wang, J., Zhu, Y., Pu, Y., Dai, W., 2020a. Appl. Catal., B 277, 119122.
Zhang, H., Nengzi, L.C., Wang, Z., Zhang, X., Li, B., Cheng, X., 2020b. J. Hazard Mater. 383, 121236.
Zhang, Z., Chen, X., Zhang, H., Liu, W., Zhu, W., Zhu, Y., 2020c. Adv. Mater. 32.
Zhou, Y., Zhou, L., Zhou, Y., Xing, M., Zhang, J., 2020. Appl. Catal., B 279, 119365.
Zhu, Y., Zhu, R., Xi, Y., Zhu, J., Zhu, G., He, H., 2019. Appl. Catal., B 255, 117739.